Acta Crystallographica Section A
Foundations of Crystallography
ISSN 0108-7673

Received 25 July 2012
Accepted 1 March 2013

© 2013 International Union of Crystallography
Printed in Singapore – all rights reserved

Nonlocality in spherical-aberration-corrected HAADF STEM images

Masahiro Ohtsuka,[a]*‡ Takashi Yamazaki,[b] Yasutoshi Kotaka,[b] Hironori Fujisawa,[c] Masaru Shimizu,[c] Koichiro Honda,[b] Iwao Hashimoto[a] and Kazuto Watanabe[d]

[a]Department of Physics, Tokyo University of Science, Tokyo 162-8601, Japan, [b]Device and Materials Laboratories, Fujitsu Laboratories Ltd, Atsugi 243-0197, Japan, [c]Graduate School of Engineering, University of Hyogo, Hyogo 671-2280, Japan, and [d]Tokyo Metropolitan College of Industrial Technology, Tokyo 140-0011, Japan. Correspondence e-mail: m-ohtsuka@nucl.nagoya-u.ac.jp

Nonlocality in spherical-aberration-corrected high-angle annular dark-field (HAADF) scanning transmission electron microscope (STEM) images is theoretically and experimentally examined using the absorption potential describing thermal diffuse scattering (TDS). A detailed comparison between the simulated and the experimentally obtained high-quality HAADF STEM images of an Si(110) bulk structure and a $PbTiO_3(100)/SrTiO_3(100)$ interfacial structure unambiguously demonstrates the need to use a nonlocal TDS absorption potential. The nonlocality in the TDS absorption potential cannot be ignored in a detailed analysis of spherical-aberration-corrected HAADF STEM images of materials consisting of several heavy elements, although it can be completely disregarded for those consisting of only light elements.

1. Introduction

Over the last few decades, continual device miniaturization has been a constant pursuit in the electronics industry, stimulating interest in the development of new materials that can be manufactured on the nanometer scale. In accordance with this trend, high-angle annular dark-field (HAADF) scanning transmission electron microscopy (STEM) has arisen as an imaging method that is widely used in both academic and industrial research fields as one of the most powerful nanometer-scale analysis techniques available. Atomic resolution HAADF STEM images have two main advantages: the images never exhibit a contrast reversal due to the sample thickness and the defocus value of the probe-forming lens, except in the eccentric defocus range (Watanabe, Yamazaki, Kikuchi *et al.*, 2001); and bright spots in images may be straightforwardly mapped to projected atomic columns (Watanabe, Yamazaki, Kikuchi *et al.*, 2001; Kotaka, 2010). Under conditions where the annular dark-field (ADF) detector is adjusted to a suitable high-angle detection range, HAADF STEM images are formed predominantly by incoherent thermal diffuse scattering (TDS) electrons, while Bragg scattering electrons are minimized. Accordingly, the HAADF STEM image intensity depends strongly on the composition and density (*i.e.* effective atomic number Z) of the target material, and thus such images are often called Z-contrast images (Pennycook & Jesson, 1990).

Recently, the development of a spherical aberration (C_s) correction technique has led to the availability of small and fine incident convergent beam probes, making possible STEM spatial resolutions in the sub-angstrom range (Haider *et al.*, 1998; Dellby *et al.*, 2001; Batson *et al.*, 2002; Hutchison *et al.*, 2002; Sawada *et al.*, 2005; Kuramochi *et al.*, 2010). In addition to the improvement in spatial resolution, spherical aberration correction leads to higher-quality images. As a result, the types of elements and number of atoms that compose individual atomic columns can be directly interpreted from the bright spot contrast at a qualitative or semi-quantitative level (Falke *et al.*, 2004; Sato *et al.*, 2006; Li *et al.*, 2007; Shibata *et al.*, 2007; Tanaka *et al.*, 2008; Smith, 2008; LeBeau *et al.*, 2010*a*), without the use of complicated image-processing techniques (Watanabe *et al.*, 2002; Nakanishi *et al.*, 2006). However, individual bright spot intensities and the background intensity change slightly, depending on the sample thickness, the defocus shift of the probe (Kotaka, 2010) *etc.* To reveal complicated crystal structures and the sample composition, a detailed analysis is required, where these variations can be compared with theoretical simulations based on the dynamical diffraction theory of high-energy electrons. For this analysis, high-quality experimental images and accurate simulations are indispensable.

The essential challenge in simulating HAADF STEM images is evaluating the contribution from incoherent

‡ Present address: Department of Materials, Physics and Energy Engineering, Graduate School of Engineering, Nagoya University, Nagoya 464-8603, Japan.

TDS events. Two distinct approaches to address this challenge have been developed: the frozen-phonon approach and the absorption potential approach. In the frozen-phonon approach, high-energy incident electrons are considered to observe frozen atoms, each with a particular thermal displacement from their equilibrium position. The detected signal is evaluated as the summation of electron intensities in the detector region, calculated for different atomic configurations, without distinction between TDS and elastic scattering (Loane *et al.*, 1991; Kirkland, 1998; Muller *et al.*, 2001). The results of the frozen-phonon approach show good agreement with the HAADF STEM images (LeBeau *et al.*, 2008). The effect of multiple thermal scattering, which becomes important for thicker specimens, can be easily incorporated into the model (LeBeau *et al.*, 2009), although the frozen-phonon calculation is a very tedious task. In the absorption potential approach, an absorption potential is introduced into the time-independent Schrödinger equation using standard simulation methods such as the Bloch-wave (Bethe, 1928; Fujimoto, 1959; Hirsch *et al.*, 1965; Humphreys, 1979) and multislice formalisms (Cowley & Moodie, 1957; Van Dyck, 1980; Ishizuka, 1982). This calculation describes absorption for elastic scattering electrons due to the effect of inelastic scattering events, based on the coupled channel Schrodinger equations (Yoshioka, 1957). The amount of TDS electrons collected by the detector is then inferred from the absorbed electrons (Pennycook & Jesson, 1991; Watanabe, Yamazaki, Hashimoto & Shiojiri, 2001; Ishizuka, 2002; Allen *et al.*, 2003). The absorption potential method using the single inelastic scattering and kinematical approximations performs well for thin crystal samples.

Currently, the simulation of core-loss imaging using STEM suggests that nonlocal effects tend to be most significant when the inner semi-angle of the detector is small and the incident convergent-beam semi-angle is large (Allen *et al.*, 2006). This situation is believed to arise from a balance wherein a large incident convergent-beam semi-angle increases the nonlocality whereas a large detector inner semi-angle, for the collection of core-loss electrons, mainly decreases the nonlocality. In general, a local approximation that ignores nonlocality in the absorption potential is considered adequate for HAADF STEM images because of the large inner semi-angle of the detector (Rez, 2000; Rossouw *et al.*, 2003; Allen *et al.*, 2006). However, it is not experimentally clear whether this approximation is valid since low-quality experimental HAADF STEM images cannot be used to identify small differences in the contrast between individual atomic columns.

In §2 of this paper we discuss nonlocality in HAADF STEM images from the viewpoint of geometrical absorption potential calculations. In §3 the experimental procedure and simulations are presented. A detailed comparison between high-quality experimental images of Si(110) and $PbTiO_3(100)/SrTiO_3(100)$ interfacial structures and their simulated equivalents is described in §4, leading to a discussion of the nonlocality observed from this comparison. Finally, the conclusion is provided in §5.

2. Theory

2.1. Absorption potential

In the absorption potential approach based on Yoshioka's coupled channel equation (Yoshioka, 1957), the effects of inelastic scattering events are perturbatively included as the absorption of elastically scattered electrons. In the Bloch-wave formalism, an elastic scattering wavefunction including absorption of the convergent-beam illumination located at $\mathbf{R}_0$ is

$$\begin{aligned}\Psi(\mathbf{R},\mathbf{R}_0,t) = \int A(\mathbf{K})\sum_j \varepsilon^j(\mathbf{K})\sum_g C_g^j(\mathbf{K}) \\ \times \exp\{i[\mathbf{K}\cdot(\mathbf{R}-\mathbf{R}_0)+\mathbf{g}\cdot\mathbf{R}+k_z^j(\mathbf{K})t]\} \\ \times \exp[-\mu^j(\mathbf{K})t]\exp[-iW(\mathbf{K})]\,\mathrm{d}\mathbf{K},\end{aligned} \quad (1)$$

where $\mathbf{R}$ is a two-dimensional position vector in a plane parallel to the entrance surface, t is the depth from the entrance surface, $\mathbf{K}$ is the surface-parallel component of a partial incident plane wave with wavevector $\mathbf{k}$, and $\varepsilon^j(\mathbf{K})$ is the excitation amplitude of the jth Bloch state. $C_g^j(\mathbf{K})$ are the Bloch-wave coefficients for Bragg reflection $\mathbf{g}$, $k_z^j(\mathbf{K})$ is the surface-normal component of wavevector $\mathbf{k}^j$ of the jth Bloch state, $\mu^j(\mathbf{K})$ is the absorption coefficient of the jth Bloch state, and $W(\mathbf{K})$ is the lens aberration function. The aperture function $A(\mathbf{K})$ is defined as

$$A(\mathbf{K}) = \begin{cases} 1, & |\mathbf{K}| \le |\mathbf{k}|\sin\alpha, \\ 0, & \text{otherwise}, \end{cases}$$

where α is the semi-angle of the entrance aperture. The attenuated elastic scattering wavefunction due to inelastic absorption effects can be derived by solving Bethe's dispersion equation (Bethe, 1928) including an absorption potential, as follows,

$$[\mathbf{k}^2-(\mathbf{k}^j+\mathbf{g})^2]C_g^j(\mathbf{K}) + (2m_0/\hbar^2)\sum_h (V_{g-h}+iU_{g,h})C_h^j(\mathbf{K}) = 0, \quad (2)$$

where V_{g-h} are the Fourier coefficients of the crystal potential associated with elastic scattering, and $U_{g,h}$ are the Fourier coefficients of the absorption potential associated with inelastic scattering. m_0 is the electron rest mass. In the real-space form, the absorption potential can be written as

$$U(\mathbf{r},\mathbf{r}') = \sum_g\sum_h \exp[i(\mathbf{k}+\mathbf{g})\cdot\mathbf{r}]U_{g,h}\exp[-i(\mathbf{k}+\mathbf{h})\cdot\mathbf{r}']. \quad (3)$$

It should be noted that this potential has a complicated nonlocal quantity associated with the two positions $\mathbf{r}$ and $\mathbf{r}'$. As a simplification, $U(\mathbf{r},\mathbf{r}')$ is considered to be local by replacing $U(\mathbf{r},\mathbf{r}')$ with $U(\mathbf{r})\delta(\mathbf{r}-\mathbf{r}')$, thus deriving the Fourier coefficients of the local absorption potential as

$$\begin{aligned}U_{g,h} &= \iint \exp[-i(\mathbf{k}+\mathbf{g})\cdot\mathbf{r}]U(\mathbf{r})\delta(\mathbf{r}-\mathbf{r}')\exp[i(\mathbf{k}+\mathbf{h})\cdot\mathbf{r}']\,\mathrm{d}\mathbf{r}\,\mathrm{d}\mathbf{r}' \\ &= \int U(\mathbf{r})\exp[-i(\mathbf{g}-\mathbf{h})\cdot\mathbf{r}]\,\mathrm{d}\mathbf{r} = U_{g-h,0}.\end{aligned} \quad (4)$$

In this local approximation the Fourier coefficient $U_{g,h}$ is equivalent to $U_{g-h,0}$. It is noted that the nonlocality does not mean the delocalization as introduced by Oxley *et al.* (2005).

2.2. TDS signal collected by an ADF detector

An exact treatment of TDS is a very tedious and time-consuming task. When the Einstein model, in which individual atoms are treated as independent harmonic oscillators, is used, the nonlocal absorption potential of TDS has the practical form (Hall & Hirsch, 1965; Radi, 1970; Bird & King, 1990; Allen & Rossouw, 1990; Weickenmeier & Kohl, 1998; Martin *et al.*, 2009)

$$U_{g,h} = (\hbar^2/2m_0)(4\pi/\Omega)\sum_\kappa f_\kappa^{\rm TDS}(\mathbf{g},\mathbf{h},M_\kappa) \times \exp[-i(\mathbf{g}-\mathbf{h})\cdot\mathbf{r}_\kappa]\exp[-M_\kappa|\mathbf{g}-\mathbf{h}|^2], \quad (5)$$

where Ω is the unit-cell volume. The position vector $\mathbf{r}_\kappa$ and $M_\kappa = 1/2\langle u_\kappa^2\rangle$ denote the equilibrium position and Debye–Waller factor, respectively, for a particular atom κ, $\langle u_\kappa^2\rangle$ being the corresponding mean-square thermal displacement. The coefficient $f_\kappa^{\rm TDS}(\mathbf{g},\mathbf{h},M_\kappa)$ is the nonlocal absorptive form factor, which is similar to what is often referred to as the mixed dynamic form factor (see, for example, Kohl & Rose, 1985; Wang, 1995; Allen *et al.*, 2003), and describes the effect of TDS on absorption due to interactions between the diffraction components $\mathbf{g}$ and $\mathbf{h}$. The nonlocal absorptive form factor of TDS is given by

$$f_\kappa^{\rm TDS}(\mathbf{g},\mathbf{h},M_\kappa) = (\gamma^2/k)\int {\rm d}\mathbf{k}'\,\delta(|\mathbf{k}|-|\mathbf{k}'|)\,f_\kappa(|\mathbf{k}'-\mathbf{k}-\mathbf{g}|) \times f_\kappa(|\mathbf{k}'-\mathbf{k}-\mathbf{h}|)\big[1-\exp\big(M_\kappa|\mathbf{g}-\mathbf{h}|^2 - M_\kappa|\mathbf{k}'-\mathbf{k}-\mathbf{g}|^2 - M_\kappa|\mathbf{k}'-\mathbf{k}-\mathbf{h}|^2\big)\big], \quad (6)$$

where $\mathbf{k}'$ is the wavevector of TDS electrons, and $\gamma = m/m_0$ is the relativistic factor, m being the relativistic electron mass. The coefficient $f_\kappa(|\mathbf{q}|)$ is the electron atomic scattering factor for momentum transfer $h\mathbf{q}$ under the first-order Born approximation. The term $\delta(|\mathbf{k}|-|\mathbf{k}'|)$ restricts the integration range to the surface of the Ewald sphere. For further simplification a high-energy approximation is made, whereby the Ewald sphere surface is assumed to be an infinite plane projected parallel to the entrance surface of the crystal,

$$f_\kappa^{\rm TDS}(\mathbf{g},\mathbf{h},M_\kappa) \approx (\gamma^2/k)\int_0^\infty K'\,{\rm d}K'\int_0^{2\pi}{\rm d}\varphi \times f_\kappa(|\mathbf{K}'-\mathbf{K}-\mathbf{g}|)f_\kappa(|\mathbf{K}'-\mathbf{K}-\mathbf{h}|) \times\big[1-\exp\big(M_\kappa|\mathbf{g}-\mathbf{h}|^2 - M_\kappa|\mathbf{K}'-\mathbf{K}-\mathbf{g}|^2 - M_\kappa|\mathbf{K}'-\mathbf{K}-\mathbf{h}|^2\big)\big], \quad (7)$$

where the wavevector $\mathbf{K}'$ refers to the surface-parallel component of $\mathbf{k}'$ on the approximated flat Ewald sphere. The angle φ is the azimuthal angle between $\mathbf{K}'$ and the surface normal. It should be noted that the nonlocal absorptive form factors in equations (6) and (7) describe absorption for full solid angles. Under this flat Ewald sphere approximation the absorptive form factor is a perfectly local quantity, *i.e.* there is no difference between $f_\kappa^{\rm TDS}(\mathbf{g},\mathbf{h},M_\kappa)$ and $f_\kappa^{\rm TDS}(\mathbf{g}-\mathbf{h},\mathbf{0},M_\kappa)$. Next, we consider HAADF STEM image simulations based on nonlocal absorptive form factors. In contrast to the above-mentioned nonlocal absorptive form factors due to TDS for full solid angles, nonlocal absorptive form factors for HAADF STEM images must include an evaluation of partial absorption due to TDS electrons collected by the ADF detector. Therefore, the shape and position of the detector must be considered in nonlocal absorptive form factor calculations. The resulting nonlocal absorptive form factor that accounts for partial absorption due to TDS electrons collected by the detector is expressed as

$$f_\kappa^{\rm TDS}(\mathbf{K},\mathbf{g},\mathbf{h},M_\kappa) = (\gamma^2/k)\int_{k\sin(\beta_{\rm inner})}^{k\sin(\beta_{\rm outer})} K'\,{\rm d}K'\int_0^{2\pi}{\rm d}\varphi \times f_\kappa(|\mathbf{K}'-\mathbf{K}-\mathbf{g}|)f_\kappa(|\mathbf{K}'-\mathbf{K}-\mathbf{h}|) \times\big[1-\exp\big(M_\kappa|\mathbf{g}-\mathbf{h}|^2 - M_\kappa|\mathbf{K}'-\mathbf{K}-\mathbf{g}|^2 - M_\kappa|\mathbf{K}'-\mathbf{K}-\mathbf{h}|^2\big)\big], \quad (8)$$

where $\beta_{\rm inner}$ and $\beta_{\rm outer}$ are, respectively, the inner and outer semi-angles of the ADF detector range. The integrand is calculated within the detector region, as shown in Fig. 1. This absorptive form factor depends on the incident wavevector $\mathbf{k}$; thus, the absorption potential has $\mathbf{k}$-dependence through the detector shape and position. The formalism proposed by Watanabe *et al.* (Watanabe, Yamazaki, Hashimoto & Shiojiri, 2001; Yamazaki *et al.*, 2006) is used to define three types of absorption potential: the absorption potential $U_{g,h}^{\rm all}(\mathbf{K})$, which includes the total TDS absorption calculated using equation (7), $U_{g,h}^{\rm detector}(\mathbf{K})$, which includes only the detector-collected TDS absorption calculated using equation (8), and $U_{g,h}^{\rm ex}(\mathbf{K}) = U_{g,h}^{\rm all}(\mathbf{K}) - U_{g,h}^{\rm detector}(\mathbf{K})$. Two types of wavefunctions, $\Psi_{\rm all}(\mathbf{R},\mathbf{R}_0,t)$ and $\Psi_{\rm ex}(\mathbf{R},\mathbf{R}_0,t)$, are calculated with $U_{g,h}^{\rm all}(\mathbf{K})$ and $U_{g,h}^{\rm ex}(\mathbf{K})$, respectively, and are evaluated on the detector plane. The difference in total intensity between these two wavefunctions is related to the number of TDS electrons collected by the ADF detector, therefore the TDS signal of a HAADF STEM image at incident probe position $\mathbf{R}_0$ is simply given by

$$I_{\rm TDS}(\mathbf{R}_0) = \int\big|\Psi_{\rm ex}(\mathbf{R},\mathbf{R}_0,t)\big|^2{\rm d}\mathbf{R} - \int\big|\Psi_{\rm all}(\mathbf{R},\mathbf{R}_0,t)\big|^2{\rm d}\mathbf{R}. \quad (9)$$

Introducing the local approximation to the partial absorption potential, the diffracted components $\mathbf{g}$ and $\mathbf{h}$ of a partial

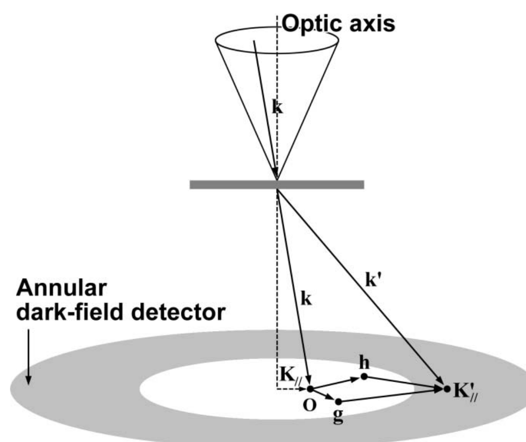

Figure 1
Schematic of the relationship between diffracted waves $\mathbf{g}$, $\mathbf{h}$ and the wavevector of TDS electrons, $\mathbf{k}'$, for an inclined partial incident plane wave with wavevector $\mathbf{k}$.

incident plane wave with wavevector **k**, which points to positions $\mathbf{K}+\mathbf{g}$ and $\mathbf{K}+\mathbf{h}$ on the flat Ewald sphere surface, are replaced by diffracted waves directed to $\mathbf{g}-\mathbf{h}$ and $\mathbf{0}$, respectively, in the calculation of equation (8). From Fig. 1, it may be inferred that the approximation is valid for low-angle scattering components but invalid when components **g** and **h** are located inside or in the vicinity of the detector. Two typical cases are considered to further elucidate this point, as shown in Fig. 2, which displays the integrands of equation (8). In the first case, the two diffracted waves are high-angle scattering components located in the vicinity of the detector region; the examples of these components are shown in Figs. 2(*a*) and 2(*b*), where Si($\bar{8}80$) and Si($\bar{7}75$) reflections for a normally incident beam ($\mathbf{K}$ = 0) are considered. The integrand is indicated under the nonlocal calculation in Fig. 2(*a*) and under the local approximation in Fig. 2(*b*). As is clear in Figs. 2(*a*) and 2(*b*), the integrand reaches significant nonzero values in the vicinity of **g** and **h**, which leads to a large integrated result from equation (8). The integrand generated using the local approximation has a smaller value in the detector region, as shown in Fig. 2(*b*), because both high-angle scattering components are simultaneously replaced by low-angle scattering components. Therefore, the local approximation underestimates the absorption potential in this case. In this example, the estimation of $U_{g,h}^{\rm detector}$ is 0.014 eV, whereas the value calculated using the nonlocal potential is 0.021 eV. The difference between the two calculations differs for various cases.

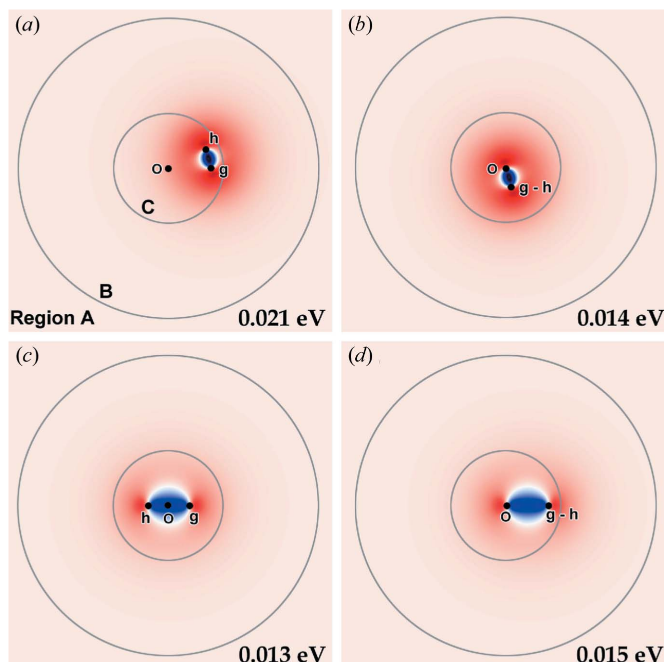

Figure 2
(*a*) The integrand in the absorptive form factor integration of an Si atom with $\langle u_\kappa^2\rangle$ = 0.0045 Å^2. The diffracted components **g** and **h** are set as Si($\bar{8}80$) and Si($\bar{7}75$) reflections, respectively, for normal-incidence conditions, *i.e.* the incident partial plane wave has $\mathbf{K}=\mathbf{0}$. The angular detection range of the detector is 67–185 mrad, which is shown as region *B*. Red and blue regions have positive and negative values, respectively. (*b*) The same integrand after applying the local approximation. The whole integrand is shifted by $-\mathbf{h}$. Parts (*c*) and (*d*) are the same as (*a*, *b*) except that the diffracted components are Si($\bar{4}40$) and Si($4\bar{4}0$) reflections, as an example of well separated middle-angle scattering components. Values of the partial absorption potential $U_{g,h}^{\rm detector}$ are shown at the bottom-right of each figure.

The second case involves two middle-angle scattering components for the Si($\bar{4}40$) and Si($4\bar{4}0$) reflection; the examples of this case are given in Figs. 2(*c*) and 2(*d*). The figures display the integrands from equation (8) for nonlocal and local calculations. In this case the local approximation changes one diffracted component into a high-angle scattering component and the other into a low-angle scattering component. The former replacement may result in overestimation, and the latter in underestimation. Thus, the value of $U_{g,h}^{\rm detector}$ is slightly overestimated, at 0.015 eV, as compared with the nonlocal equivalent, 0.013 eV. The difference between these quantities is insignificant compared with the previous example. In this example, underestimated points in the local approximation have negated the effect of overestimated points, thus the integral has been almost unaffected. In simple terms, the contribution of high-angle scattering components is larger than that of middle-angle scattering components, and hence use of the local approximation risks underestimation of the absorption potential. Therefore, bright spot contrasts in HAADF STEM images are expected to exhibit nonlocal features where the atomic columns are composed of heavier atoms, owing to the large values of $f_\kappa(|q|)$ and the strongly localized wavefield formed on the columns. This fact implies that the main feature of the nonlocality appears as the difference between individual atomic columns in HAADF STEM images.

3. Experimental procedure and simulations

An Si single crystal and $PbTiO_3/SrTiO_3$ ferroelectric interfacial material were selected to investigate the nonlocality in high-quality C_s-corrected HAADF STEM images. The Si materials were commercially obtained, and $PbTiO_3/SrTiO_3$ ferroelectric materials were fabricated on single crystals of $SrTiO_3$(100). For preparation of this material, single crystals of $SrTiO_3$ were etched in buffered NH_4F–HF solution and subsequently annealed in air. $PbTiO_3$ thin films were grown on $SrTiO_3$ substrates to a thickness of 7.8 nm by MOCVD, using $(C_2H_5)_3PbOCH_2C(CH_3)_3$ and $Ti(O\text{-}iC_3H_7)_4$ precursors, with O_2 as the oxidizing gas (Shimizu *et al.*, 2004). The film was coherently lattice matched to the substrate, and it is believed that compressive strain caused the film to polarize only in the surface normal direction (Pertsev *et al.*, 1998).

Specimens were cut into discs of 3 mm diameter, which were mechanically ground and polished to a thickness of ~100 µm and then dimpled to ~20 µm at the center of the disc. The samples were then prepared for TEM by ion milling with 5 keV Ar^+ ions at an incident angle of 4° until a tiny perforation of the central disc area occurred, followed by ion milling with 2 keV Ar^+ ions at the smallest possible incident angle in order to remove amorphous and damaged regions.

HAADF STEM observations were carried out using a JEM-2100F TEM/STEM (Jeol, Japan) microscope operated at

200 keV and equipped with a C_s-corrector (CEOS, Germany). The spherical aberration coefficient C_s of the probe-forming lens was −0.5 μm (Uhlemann & Haider, 1998). Sample thicknesses were measured by low-loss electron-energy-loss (EEL) spectra using the log-ratio method. The observation areas in two samples were selected to be of a thickness of ∼30 nm. A Gatan Enfina spectrometer with a collection aperture of 15 mrad was used to obtain EEL spectra. The semi-angle of the incident convergent beam was 20.0 mrad, and the angular detection range of the ADF detector was 67–185 mrad, which was measured using a microdiffraction method (Yamazaki *et al.*, 2002). The illumination system of the microscope was precisely aligned to achieve coma- and astigmatism-free conditions (Kuramochi, Yamazaki *et al.*, 2008). In C_s-corrected HAADF STEM images the effect of defocus spread due to chromatic aberration (C_c coefficient) and energy distribution of the incident beam cannot be ignored. The C_c coefficient was measured to be 1.72 mm from a one-frame through-focal HAADF STEM image (Kuramochi *et al.*, 2009). The standard deviation of the incident energy distribution, which was assumed to have a Gaussian form, was 1.0 eV, as measured from the shape of the zero-loss EEL spectrum. In addition to precise knowledge of optical parameters, instrumentation reliability for measures such as brightness and contrast settings must be taken into account for a detailed comparison with simulation results. The sample thicknesses were measured by both the position-averaged convergent-beam electron diffraction (PACBED) method (LeBeau *et al.*, 2010*b*) and the log-ratio method using low-loss EEL spectra. The thicknesses measured by the PACBED method have been sufficiently consistent with the results measured by the log-ratio method. The PACBED patterns are obtained directly after the acquisition of HAADF STEM images without changing optical parameters. The thicknesses were determined by comparisons with patterns calculated by the dynamical simulations. The fitting result for $SrTiO_3$ is shown in Fig. 3 as an example. The PACBED patterns matched to within ±2 nm.

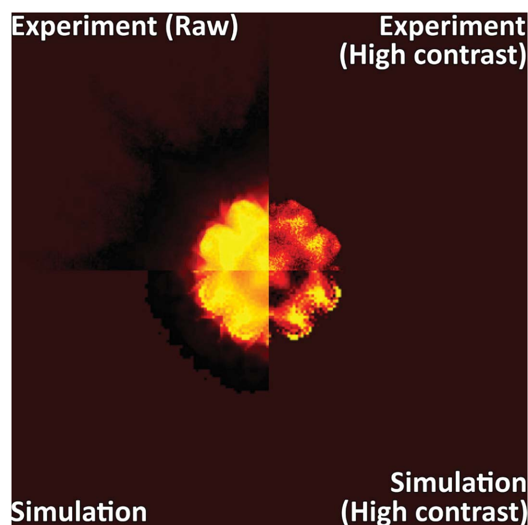

Figure 3
Comparison between experimental (left half) and simulated (right half) PACBED patterns for 30 nm-thick $SrTiO_3(001)$. The right half of this figure shows contrast-enhanced results of the left half to clarify the characteristic patterns.

It is noted that, thus far, the defocus value of the probe-forming lens and with the Gaussian broadening values (*i.e.* the spatial incoherence due to source size, sample drift) are undecided. These values are determined by finding the best match between high-quality experimental C_s-corrected HAADF STEM images and their corresponding simulations. It is noted that the Gaussian broadening is presumably not a good approximation for a perfectly quantitative analysis, since the tail of the realistic broadening shape cannot be reproduced by a Gaussian distribution (Maunders *et al.*, 2011). Noise caused by damage and surface roughness was reduced using statistical averaging, by which raw images clipped from equivalent regions were averaged based on the translational symmetry of the crystal. The experimental noise was significantly reduced using this method (Kuramochi, Suzuki *et al.*, 2008), without drastically changing the image intensity compared with the original data; such a reduction in the experimental noise was not observed using other methods such as deconvolution processing. Thus, detailed comparisons with image simulations can be made with these processed data. Here, high-quality raw HAADF STEM images indicate that the standard deviation of the atomic column intensity is less than 5% of the averaged background intensity. Hereafter, this criterion will be referred to as the ‘quality value’.

As briefly explained in §2, HAADF STEM image simulations were carried out using a Bloch-wave-based absorption potential approach developed by Watanabe *et al.* (Watanabe, Yamazaki, Hashimoto & Shiojiri, 2001; Yamazaki *et al.*, 2006). This method rapidly calculates HAADF STEM images formed by both Bragg scattering and incoherent TDS, simultaneously or separately. In the present simulation, Bloch waves were described by a plane-wave basis set belonging to zeroth-order Laue-zone reflections within a cutoff frequency of 25 nm^{-1}. It is noted that this cutoff frequency does not mean the restriction of the integration in equations (6) and (8), and their numerical integrations were carried out for defined ranges accurately. The incident convergent beams (semi-angle 20 mrad) were comprised of more than 1400 partial incident plane waves. These values are sufficiently large to describe the exact wavefields inside the sample and the incident probe functions on the entrance surface for STEM image calculations. In the image simulation of Si single crystals the mean-squared thermal vibration of Si atoms was set to 0.0045 $Å^2$ (Radi, 1970). In simulations of the $PbTiO_3/SrTiO_3$ interfacial structure a supercell composed of five fundamental $PbTiO_3$ unit cells and five fundamental $SrTiO_3$ unit cells was used; in these simulations the values of the mean-squared thermal vibration of Pb, Sr, Ti (in the $SrTiO_3$ crystal region), Ti (in the $PbTiO_3$ crystal region), O (in the $SrTiO_3$ crystal region) and O (in the $PbTiO_3$ crystal region) atoms were set to 0.00861, 0.00684, 0.00469, 0.00456, 0.00709 and 0.00735 $Å^2$, respectively (Joseph *et al.*, 2000; Kiat *et al.*, 2000). The effects of lattice distortion and the mixing concentration of Sr and Pb near the interface were taken into account in the above-

mentioned supercell model. These interfacial structure models were roughly modeled with lattice distortion and mixing concentration by a detailed matching between the intensity profiles of the experimental HAADF STEM image and the corresponding simulation (Kuramochi, Suzuki *et al.*, 2008).

4. Results and discussions

Recently, a method for placing experimental images on an absolute intensity scale has been proposed (LeBeau & Stemmer, 2008) for a more quantitative comparison between experimental C_s-uncorrected HAADF STEM images and image simulations (LeBeau *et al.*, 2008). However, a specialized instrument having a detector with a very large dynamic range is required to perform a detailed comparison based on the absolute intensity between C_s-corrected experiments and simulations, because of its very high current electron beam. As the main influence of the nonlocality is expected to be in the differences in the background-subtracted atomic column intensities, the influence of the nonlocality can be largely discussed using a detailed comparison based on the image contrast. Thus, we have carried out a detailed comparison based on image contrast, subtracting the background intensity at interatomic column positions and scaling particular experimental atomic column intensities to the corresponding simulated ones.

First, the HAADF STEM image of an Si single crystal is examined, as an example of a crystal composed of a single light element. Fig. 4(*a*) shows the experimental HAADF STEM image of an Si single crystal recorded along the [110] direction, together with its image processed using statistical averaging (Kuramochi, Suzuki *et al.*, 2008). The quality value of this experimental image was less than 5%. The sample thickness was measured to be 33 nm. Image simulations of this crystal were carried out for two types of absorption potentials: the nonlocal TDS absorption potential and the local equivalent. To allow for a detailed comparison, the calculated HAADF STEM image intensities were calibrated with experimental data. The maximum and minimum intensities of the simulated images were normalized to be identical to those of the experimental data; that is, the experimental and simulated intensities at Si atomic columns are scaled to 1.0 after the background subtraction. The respective best matched images, which are superimposed in Fig. 4(*a*), were calculated with a defocus value of +8.0 nm (overfocus) and a Gaussian broadening value of 0.06 nm full width at half-maximum (FWHM) for both nonlocal and local calculations. Both calculations reproduced the experimental image quite well. Figs. 4(*b*) and 4(*c*) display a more detailed comparison, with overlaid line profiles of the three images shown in Fig. 4(*a*). Both simulations accurately reproduced the experimental intensity profile. In this case there is no discernible difference between the cases of using the nonlocal or the local absorption potential. Thus, for Si(110) images, the nonlocality can be completely disregarded.

Next, the high-quality C_s-corrected HAADF STEM image of the $PbTiO_3/SrTiO_3$ interface is discussed as an example of the imaging of combined light and heavy elements. Fig. 5(*a*) shows an experimental image of the cross-sectional view of an epitaxial $PbTiO_3$ crystal on $SrTiO_3$ substrate recorded along the [100] direction. As in Fig. 4(*a*), the processed image data and two kinds of image simulation are shown. In the experimental image the quality value was measured to be less than 5% in the $SrTiO_3$ region. The corresponding simulated HAADF STEM images were calibrated by referring to the region of the $SrTiO_3$ substrate in the experimental image; that is, the whole image intensities are normalized by scaling the Sr atomic column intensity in experimental images and simulations are scaled to 1.0 after subtracting the background intensity of the $SrTiO_3$ region. The sample thickness was 30 nm. It has been reported that

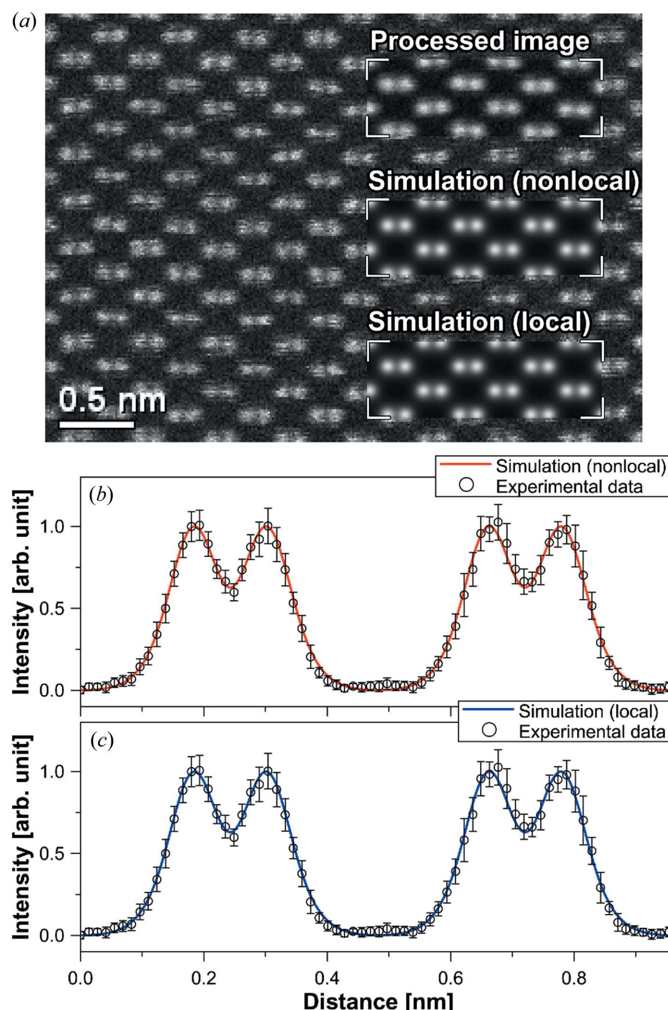

Figure 4
(*a*) Experimental HAADF STEM image of an Si bulk structure along the [110] direction, with three overlaid images: a static averaging processed image (top row), the best matched simulated image calculated using the nonlocal absorption potential (middle row), and the same but calculated using the local approximation (bottom row). (*b*) Intensity line profiles along the line intersecting the Si dumbbell structure, used for a detailed comparison between processed data and simulation using the nonlocal absorption potential. The error bars show non-systematic errors due to the statistical averaging process. (*c*) The same as (*b*) but the simulation is carried out using the local approximation.

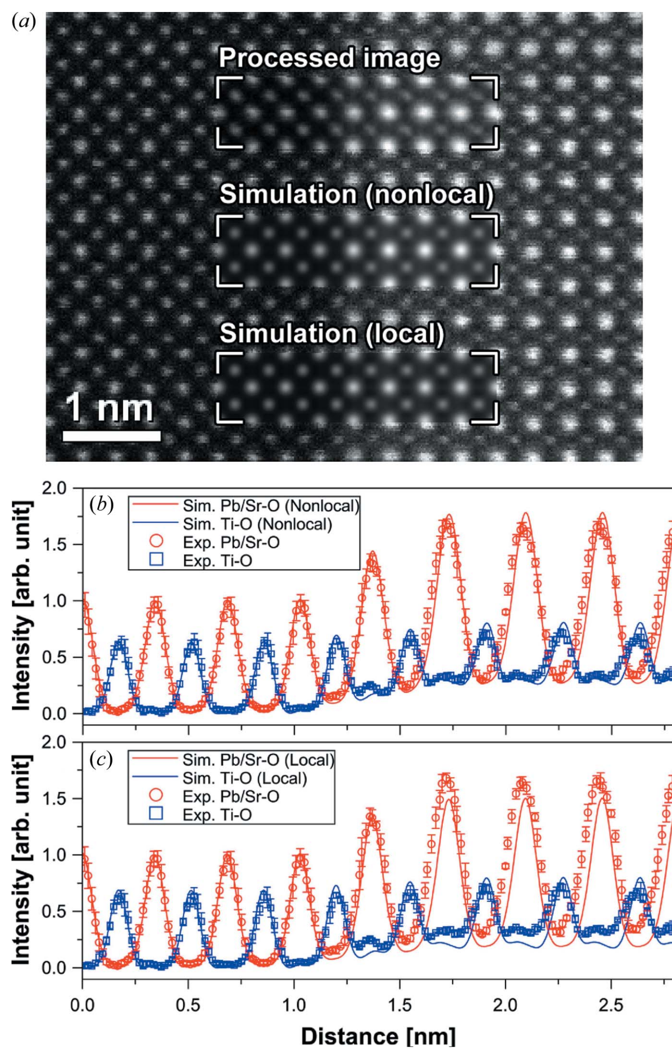

Figure 5
(*a*) Experimental HAADF STEM image of the $PbTiO_3/SrTiO_3$ interface structure with three overlaid images: static average processed image (top row), the best matched simulated image calculated using the nonlocal absorption potential (middle row), and the same image calculated with the local approximation (bottom row). (*b*) Intensity line profiles along the line intersecting Pb/Sr and O atomic columns and Ti and O atomic columns for detailed comparison between processed data and simulation using the nonlocal absorption potential. The error bars show non-systematic errors due to the statistical averaging process. (*c*) The same as (*b*) but with the simulation carried out using the local approximation.

multiple thermal scattering can be neglected for this thickness range (LeBeau *et al.*, 2009). The lower intensity of Pb atomic columns at the first atomic layer of the $PbTiO_3$ region as compared with that at subsequent layers is reproduced by a simple mixing model in which 80% of Pb atoms are substituted by Sr atoms. The smaller peak spacing between the first and second Pb—O atomic layers as compared with that between subsequent layers is caused by 5% compressive strain in the surface normal direction for the first $PbTiO_3$ lattice well.

In contrast to the Si single crystal, two undecided parameters in two types of simulations were determined by image matching in the $SrTiO_3$ region. In the simulation using the nonlocal absorption potential, a −6.0 nm defocus value (underfocus) and 0.08 nm FWHM Gaussian broadening of the image were the best-fit parameters. Gaussian broadening in the local absorption potential calculation was attributed to the nonlocal case. However, the best-fit defocus value for the local calculation was −10.0 nm (underfocus). Both absorption potentials seem to reproduce both bulk regions as well as the interface. Figs. 5(*b*) and 5(*c*) display line profiles from the overlaid images in Fig. 5(*a*) across the Pb and O atomic columns and across the Ti and O atomic columns of the interface, as well as in the $SrTiO_3$ and $PbTiO_3$ regions. Fig. 5(*b*) shows that the nonlocal absorption potential perfectly reproduces the experimental intensity profiles at the interface and in the $PbTiO_3$ and $SrTiO_3$ regions. However, the local absorption potential does not match the intensity profiles for the interface or $PbTiO_3$ regions, although the intensity profile in the $SrTiO_3$ region matches quite well, as shown in Fig. 5(*c*). The intensities are lower in the inter-column positions and Pb column positions. This observation supports the view of nonlocal effects in HAADF STEM images discussed in §2, namely that heavier atomic columns, in particular, show nonlocality because of the large value of $f_\kappa(|q|)$ for heavier atoms. It is noted that a best-matched simulation for only the $PbTiO_3$ region could be obtained using the local absorption potential with different defocus and Gaussian broadening values. Because of this freedom in fitting, it is difficult to determine the degree of nonlocality from matching between only one HAADF STEM image and its corresponding simulation. A best-matched HAADF STEM image simulation can be obtained using other values for the calculation parameters, especially for materials containing a single element or several elements with a small difference in atomic number. In any case, use of the local absorption potential approximation invites errors in the estimation of crystal structure composition.

5. Conclusions

The effect of the nonlocality in a C_s-corrected HAADF STEM image has been discussed in detail. Clear evidence for absorption potential nonlocality has been presented for Pb atomic columns in a high-quality modern C_s-corrected HAADF STEM image of an $SrTiO_3(100)/PbTiO_3(100)$ interface structure. This was determined by detailed comparison between high-quality experimental images and corresponding simulated images. On the other hand, it was found that nonlocality could be safely ignored in an Si(110) image. Hence, nonlocality cannot always be disregarded in the detailed analysis of C_s-corrected HAADF STEM images, although the relation between structure and image is straightforward. The validity of the local approximation in a high-quality HAADF STEM image depends on the sample composition. Therefore, nonlocality cannot be ignored in the quantitative analysis of C_s-corrected HAADF STEM images for a material composed of heavier elements or for complicated structures such as interfaces.

References

Allen, L. J., Findlay, S. D., Oxley, M. P. & Rossouw, C. J. (2003). *Ultramicroscopy*, **96**, 47–63.
Allen, L. J., Findlay, S. D., Oxley, M. P., Witte, C. & Zaluzec, N. J. (2006). *Ultramicroscopy*, **106**, 1001–1011.
Allen, L. J. & Rossouw, C. J. (1990). *Phys. Rev. B*, **42**, 11644–11654.
Batson, P. E., Dellby, N. & Krivanek, O. L. (2002). *Nature (London)*, **418**, 617–620.
Bethe, H. A. (1928). *Ann. Phys. (Leipzig)*, **87**, 55–129.
Bird, D. M. & King, Q. A. (1990). *Acta Cryst.* A**46**, 202–208.
Cowley, J. M. & Moodie, A. F. (1957). *Acta Cryst.* **10**, 609–619.
Dellby, N., Krivanek, O. L., Nellist, P. D., Batson, P. E. & Lupini, A. R. (2001). *J. Electron Microsc.* **50**, 177–185.
Falke, U., Bleloch, A., Falke, M. & Teichert, S. (2004). *Phys. Rev. Lett.* **92**, 116103.
Fujimoto, F. (1959). *J. Phys. Soc. Jpn*, **14**, 1558–1568.
Haider, M., Uhlemann, S., Schwan, E., Rose, H., Kabius, B. & Urban, K. (1998). *Nature (London)*, **392**, 768–769.
Hall, C. R. & Hirsch, P. B. (1965). *Proc. R. Soc. London A*, **286**, 158–177.
Hirsch, P. B., Howie, A., Nicholson, P. B., Pashley, D. W. & Whelan, M. J. (1965). *Electron Microscopy of Thin Crystals.* London: Butterworths.
Humphreys, C. J. (1979). *Rep. Prog. Phys.* **42**, 1825–1887.
Hutchison, J. L., Titchmarsh, J. M., Cockayne, D. J. H., Mobus, G., Hetherington, C. J., Doole, R. C., Hosokawa, F., Hartel, P. & Haider, M. (2002). *Microsc. Microanal.* **8**, 10–11.
Ishizuka, K. (1982). *Acta Cryst.* A**38**, 773–779.
Ishizuka, K. (2002). *Ultramicroscopy*, **90**, 71–83.
Joseph, J., Vimala, T. M., Sivasubramanian, V. & Murthy, V. R. K. (2000). *J. Mater. Sci.* **35**, 1571–1575.
Kiat, J.-M., Baldinozzi, G., Dunlop, M., Malibert, C., Dkhil, B., Menoret, C., Masson, O. & Fernandez-Diaz, M. T. (2000). *J. Phys. Condens. Matter*, **12**, 8411–8425.
Kirkland, E. J. (1998). *Advanced Computing in Electron Microscopy.* New York: Plenum Press.
Kohl, H. & Rose, H. (1985). *Adv. Electron. Electron Phys.* **65**, 173–227.
Kotaka, Y. (2010). *Ultramicroscopy*, **110**, 555–562.
Kuramochi, K., Kotaka, Y., Yamazaki, T., Ohtsuka, M., Hashimoto, I. & Watanabe, K. (2010). *Acta Cryst.* A**66**, 10–16.
Kuramochi, K., Suzuki, K., Yamazaki, T., Mitsuishi, K., Furuya, K., Hashimoto, I. & Watanabe, K. (2008). *Ultramicroscopy*, **109**, 96–103.
Kuramochi, K., Yamazaki, T., Kotaka, Y., Kikuchi, Y., Hashimoto, I. & Watanabe, K. (2008). *Ultramicroscopy*, **108**, 339–345.
Kuramochi, K., Yamazaki, T., Kotka, Y., Ohtsuka, M., Hashimoro, I. & Watanabe, K. (2009). *Ultramicroscopy*, **110**, 36–42.
LeBeau, J. M., Findlay, S. D., Allen, L. J. & Stemmer, S. (2008). *Phys. Rev. Lett.* **100**, 206101.
LeBeau, J. M., Findlay, S. D., Allen, L. J. & Stemmer, S. (2010*a*). *Nano Lett.* **10**, 4405–4408.
LeBeau, J. M., Findlay, S. D., Allen, L. J. & Stemmer, S. (2010*b*). *Ultramicroscopy*, **110**, 118–125.
LeBeau, J. M., Findlay, S. D., Wang, X., Jacobson, A. J., Allern, L. J. & Stemmer, S. (2009). *Phys. Rev. B*, **79**, 214110.
LeBeau, J. M. & Stemmer, S. (2008). *Ultramicroscopy*, **108**, 1653–1658.
Li, Z. Y., Young, N. P., Vece, M. D., Palomba, S., Palmer, R. E., Bleloch, A. L., Curley, B. C., Johnston, R. L., Jiang, J. & Yuan, J. (2007). *Nature (London)*, **451**, 46–48.
Loane, R. F., Xu, P. & Silcox, J. (1991). *Acta Cryst.* A**47**, 267–278.
Martin, A. V., Findlay, S. D. & Allen, L. J. (2009). *Phys. Rev. B*, **80**, 024308.
Maunders, C., Dwyer, C., Tiemeijer, P. C. & Etheridge, J. (2011). *Ultramicroscopy*, **111**, 1437–1446.
Muller, D. A., Edwards, B., Kirkland, E. J. & Silcox, J. (2001). *Ultramicroscopy*, **86**, 371–380.
Nakanishi, N., Kotaka, Y. & Yamazaki, T. (2006). *Ultramicrosopy*, **106**, 889–901.
Oxley, M. P., Cosgriff, E. C. & Allen, L. J. (2005). *Phys. Rev. Lett.* **94**, 203906.
Pennycook, S. J. & Jesson, D. E. (1990). *Phys. Rev. Lett.* **64**, 938–941.
Pennycook, S. J. & Jesson, D. E. (1991). *Ultramicroscopy*, **37**, 14–38.
Pertsev, N. A., Zembilgotov, A. G. & Tagantsev, A. K. (1998). *Phys. Rev. Lett.* **80**, 1988–1991.
Radi, G. (1970). *Acta Cryst.* A**26**, 41–56.
Rez, P. (2000). *Ultramicroscopy*, **81**, 195–202.
Rossouw, C. J., Allen, L. J., Findlay, S. D. & Oxley, M. P. (2003). *Ultramicroscopy*, **96**, 299–312.
Sato, Y., Buban, J. P., Mizoguchi, T., Shibata, N., Yodogawa, M., Yamamoto, T. & Ikuhara, Y. (2006). *Phys. Rev. Lett.* **97**, 106802.
Sawada, H., Tomita, T., Naruse, M., Honda, T., Hambridge, P., Hartel, P., Haider, M., Hetherington, C., Doole, R., Kirkland, A., Hutchison, J., Titchmarsh, J. & Cockayne, D. (2005). *J. Electron Microsc.* **54**, 119–121.
Shibata, N., Chisholm, M. F., Nakamura, A., Pennycook, S. J., Yamamoto, T. & Ikuhara, Y. (2007). *Science*, **316**, 82–85.
Shimizu, M., Okaniwa, M., Fujisawa, H. & Niu, H. (2004). *J. Eur. Ceram. Soc.* **24**, 1625–1628.
Smith, D. J. (2008). *Microsc. Microanal.* **14**, 2–15.
Tanaka, N., Cho, S. P., Shklyaev, A. A., Yamasaki, J., Okunishi, E. & Ichikawa, M. (2008). *Appl. Surf. Sci.* **254**, 7569–7572.
Uhlemann, S. & Haider, M. (1998). *Ultramicroscopy*, **72**, 109–119.
Van Dyck, D. (1980). *J. Microsc.* **119**, 141–152.
Wang, Z. L. (1995). *Elastic and Inelastic Scattering in Electron Diffraction and Imaging.* New York: Plenum Press.
Watanabe, K., Kotaka, Y., Nakanishi, N., Yamazaki, T., Hashimoto, I. & Shiojiri, M. (2002). *Ultramicroscopy*, **92**, 191–199.
Watanabe, K., Yamazaki, T., Hashimoto, I. & Shiojiri, M. (2001). *Phys. Rev. B*, **64**, 115432.
Watanabe, K., Yamazaki, T., Kikuchi, Y., Kotaka, Y., Kawasaki, M., Hashimoto, I. & Shiojiri, M. (2001). *Phys. Rev. B*, **63**, 085315.
Weickenmeier, A. L. & Kohl, H. (1998). *Acta Cryst.* A**54**, 283–289.
Yamazaki, T., Kawasaki, M., Watanabe, K., Hashimoto, I. & Shiojiri, M. (2002). *Ultramicroscopy*, **92**, 181–189.
Yamazaki, T., Watanabe, K., Kuramochi, K. & Hashimoto, I. (2006). *Acta Cryst.* A**62**, 233–236.
Yoshioka, H. (1957). *J. Phys. Soc. Jpn*, **12**, 618–628.